Supplementary Information

High-entropy superparaelectrics with locally diverse ferroic distortion for high-capacitive energy storage

Jianhong Duan[1], Kun Wei[1], Qianbiao Du[1], Linzhao Ma[1], Huifen Yu[2], He Qi[2]*, Gaokuo Zhong[3]* and Hao Li[1]*

[1]College of Electrical and Information Engineering, Hunan University, Changsha 410082, China

[2]Beijing Advanced Innovation Center for Materials Genome Engineering Department of Physical Chemistry, University of Science and Technology Beijing, Beijing 100083, China

[3]Shenzhen Institute of Advanced Technology, Chinese Academy of Sciences, Shenzhen 518055, China

*Corresponding author, E-mail: qiheustb@ustb.edu.cn; gk.zhong@siat.ac.cn; hli@hnu.edu.cn

Methods

Finite element simulation

The electric field, electric potential distribution, and electric tree evolution of SLTT-0 and SLTT-0.30 ceramics were simulated by the finite element simulation method with 2D models using COMSOL software. The simulation model and parameters were based on the yellow boxed area of the SEM image shown in Supplementary Fig. 11. A scalar field $s(x,t)$ is used to represent the breakdown state (where $s = 1$ for the initial state and $s = 0$ for the complete breakdown state; $0 \leq s \leq 1$). As the dielectric constant (ε_r) is a continuous function of s, the breakdown state can be described by the difference of ε_r, which can be expressed by the following equation[1,2]:

$$\varepsilon(s) = \frac{\varepsilon_{ini}}{f(s) + \psi} \qquad (1)$$

where εini represents the initial ε_r, $f(s) = 4s^3 - 3s^4$, and ψ is 0.0001. Furthermore, the ε_r of grains is electric field-dependent in ceramics, following Johnson's approximation[3], whereas the ε_r of grain boundaries is linear. Consequently, the ε_r for grains (ε_g) and grain boundaries (ε_{gb}) at a given electric field is described by the following equation:

$$\varepsilon_{ini}(E) = \frac{\varepsilon_g(0)}{(1 + kE^2)^{1/3}} \qquad (2)$$

$$\varepsilon_{ini}(E) = \varepsilon_{gb} \qquad (3)$$

where k is 0.0013, and ε_g (0) is the zero-field dielectric constant and is taken to be 6048 and 1316 for SLTT-0 and SLTT-0.30 ceramics, respectively. In this simulation, the ratio of ε_g to ε_{gb} is set to be 10:1[4,5].The theoretical model can be established by the following equation:

$$\overline{\nabla}\left[\frac{1}{f(s) + \psi}\overline{\nabla\phi}\right] = 0 \qquad (4)$$

$$\frac{\partial s}{\partial t} = -\frac{f'(s)}{2[f(s) + \psi]^2}\overline{\nabla\phi} \times \overline{\nabla\phi} + f'(s) + \frac{1}{2}\overline{\nabla}^2 s \qquad (5)$$

Under the correct boundary and initial conditions, Equation (4) and (5) can be applied to the solution of dimensionless unknown fields $\phi(x,t)$ and $s(x,t)$. The simulation results are shown in Supplementary Fig. 7.

Supplementary Table 1 Configuration entropy (S_{config}) of the SLTT-x ceramics.

x	0	0.20	0.25	0.30	0.35
S_{config}	0.88R	1.47R	1.55R	1.61R	1.66R

S_{config} can be calculated using the following equation[6,7]:

$$S_{config} = -R((\sum_{i=1}^{N} x_i ln x_i) + (\sum_{j=1}^{M} x_j ln x_i)) \quad (6)$$

where R, N (M) and x_i (x_j) are the ideal gas constant, atomic species and contents at the equivalent cation (anion) sites, respectively. Note that the x in the SLTT-x system represents the mass ratio. Therefore, x needs to be converted to a molar ratio before it can be used to calculate S_{config}. It is defined as medium entropy when $1.0R \leq S_{config} < 1.5R$ and high entropy when $S_{config} \geq 1.5R$.

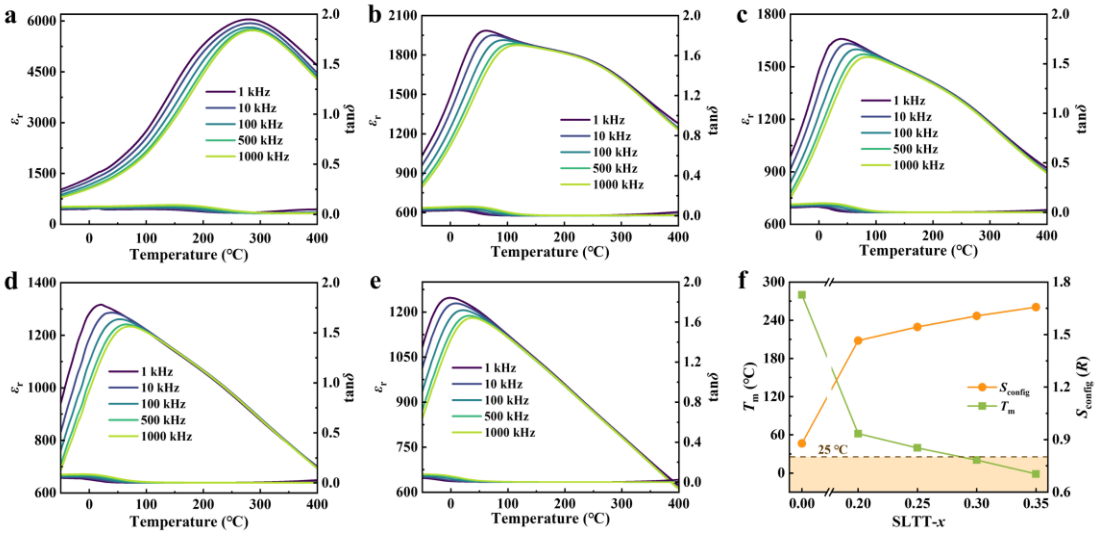

Supplementary Fig. 1 Temperature-dependence of the dielectric constant (ε_r) and loss (tanδ) at different frequencies for **a** x = 0, **b** x = 0.20, **c** x = 0.25, **d** x = 0.30, and **e** x = 0.35. **f** S_{config} and T_m as a function of x. With an increase in S_{config}, the relaxor features are visibly enhanced, manifested by the broadened dielectric peak and the pronounced frequency dispersion[8,9]. Importantly, T_m decreases significantly and is inversely related to S_{config}. As S_{config} increases from 0.88R (x = 0) to 1.61R (x = 0.30), T_m decreases correspondingly from 279.9 °C to 20.3 °C. Further increasing S_{config} to 1.66R (x = 0.35), T_m drops to –1.3 °C. This phenomenon confirms the achievement of the room temperature SPE state in SLTT-0.30 and SLTT-0.35 ceramics.

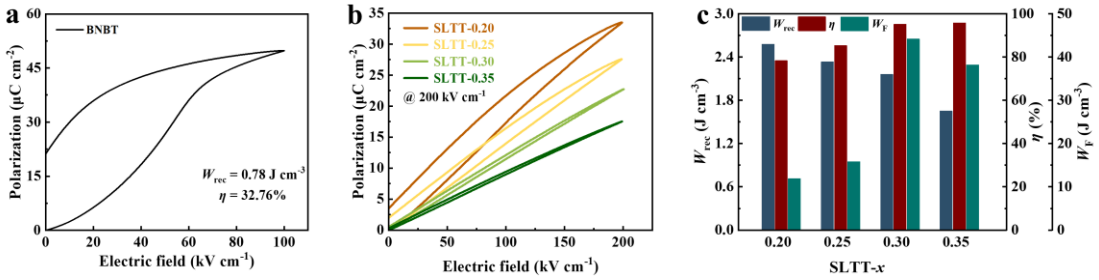

Supplementary Fig. 2 a Unipolar *P-E* loop of SLTT-0 ceramic at 100 kV cm^{-1} and 10 Hz. **b** Unipolar *P-E* loops of SLTT-*x* ceramics (*x* = 0.20, 0.25, 0.30, and 0.35) at 200 kV cm^{-1} and 10 Hz. **c** Comparison of W_{rec}, η, and W_F of SLTT-*x* ceramics (*x* = 0.20, 0.25, 0.30, and 0.35) at 200 kV cm^{-1}. The total energy density (W_{tot}), W_{rec}, and η can be calculated using the following equations[10,11]:

$$W_{tot} = \int_0^{P_m} EdP \qquad (7)$$

$$W_{rec} = \int_{P_r}^{P_m} EdP \qquad (8)$$

$$\eta = \frac{W_{rec}}{W_{tot}} \times 100\% \qquad (9)$$

Although SLTT-0 ceramic possesses a high P_m, it also has a low E_b and a large P_r, thus resulting in poor performance (W_{rec} = 0.78 J cm^{-3} and η = 32.6%). As *x* increases, the P_m, polarization switching hysteresis, and P_r under 200 kV cm^{-1} demonstrate a decreasing trend. Particularly, SLTT-0.30 and SLTT-0.35 ceramics display extremely thin *P-E* loops, indicating that the increase in S_{config} promotes the transition from RFEs to SPEs. Moreover, the RFE ceramic of SLTT-0.20 obtains a high W_{rec} of 2.58 J cm^{-3} but only a moderate η of 78.22%, resulting in a low W_F of 11.83. The SLTT-0.30 SPE reaches a W_{rec} of 2.33 J cm^{-3} while η increases to 95.11%, and thus the W_F reaches 44.17, which is 273% better than that of SLTT-0.20. The W_{rec} of SLTT-0.35 SPE decreases to 1.65 J cm^{-3} due to the large decrease of P_m to 17.51 μC cm^{-2}, so that the W_F still decreases to 38.16 even though η reaches 95.68%.

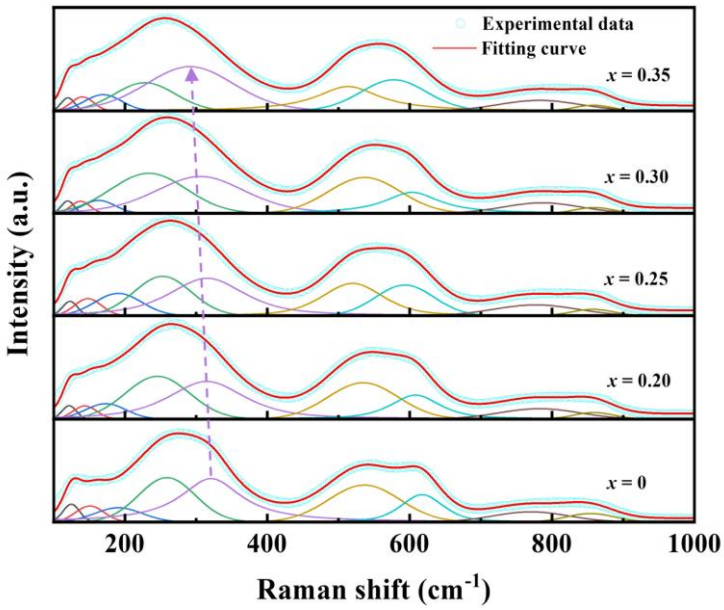

Supplementary Fig. 3 Raman spectra of the SLTT-*x* ceramics. Raman spectra (100–1000 cm^{-1}) are used to investigate the local structural variations. Four distinct regions can be observed, which are consistent with the results of previous studies[9,12]. As the SLTT content increases, the peak at ~320 cm^{-1} shifts to lower wavenumbers, indicating increased cation disorder and reduced unit cell polarity[13]. The peak intensity at ~537 cm^{-1} decreases while the peak intensity at ~617 cm^{-1} increases, which is related to the distortion of the BO_6 octahedron[14].

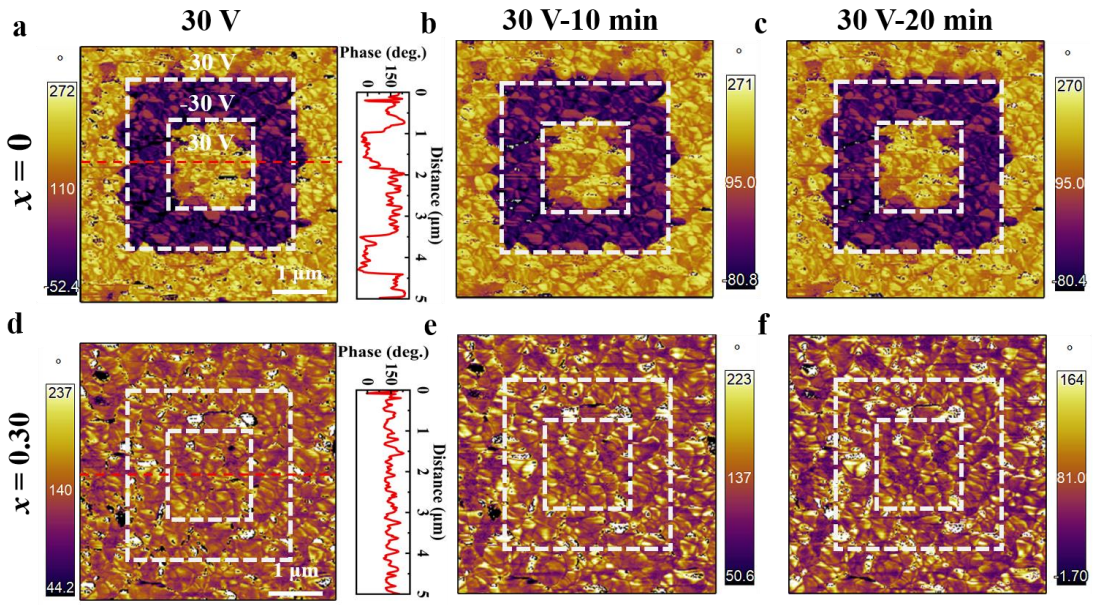

Supplementary Fig. 4 Out-of-plane PFM phase images after poling treatment and corresponding piezoresponse phase profiles generated from the line scanfor **a** $x = 0$ and **d** $x = 0.30$. Out-of-plane PFM phase images after relaxation durations for **b**, **c** $x = 0$ and **e**, **f** $x = 0.30$. Ferroelectric domain structure and corresponding phase phase signal are found in the out-of-plane PFM and phase profile of SLTT-0. These ferroelectric domains remain in an induced state even after unloading the voltage for a period of time, which is not conducive to obtaining high energy storage efficiency[9,15]. In contrast, no domain switching is detected in the SLTT-0.30 high-entropy SPE. This may be due to the fact that the high-dynamic and small-sized PNRs quickly recovered from the induced state to the initial state after unloading the voltage. The PFM images are recorded after the voltage is unloaded, so the domain switching could not be detected in time[16].

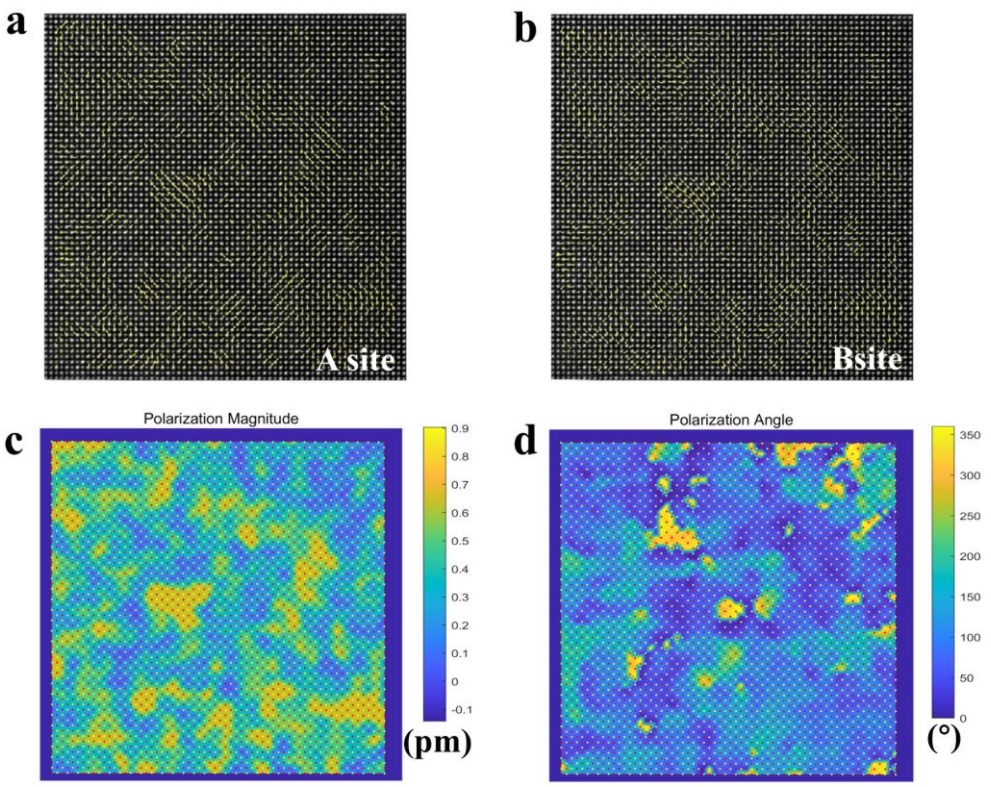

Supplementary Fig. 5 Polarization vector mappings of **a** A site and **b** B site atoms along $[100]_c$. **c** Polarization magnitude mapping and **d** polarization angle mapping along $[100]_c$.

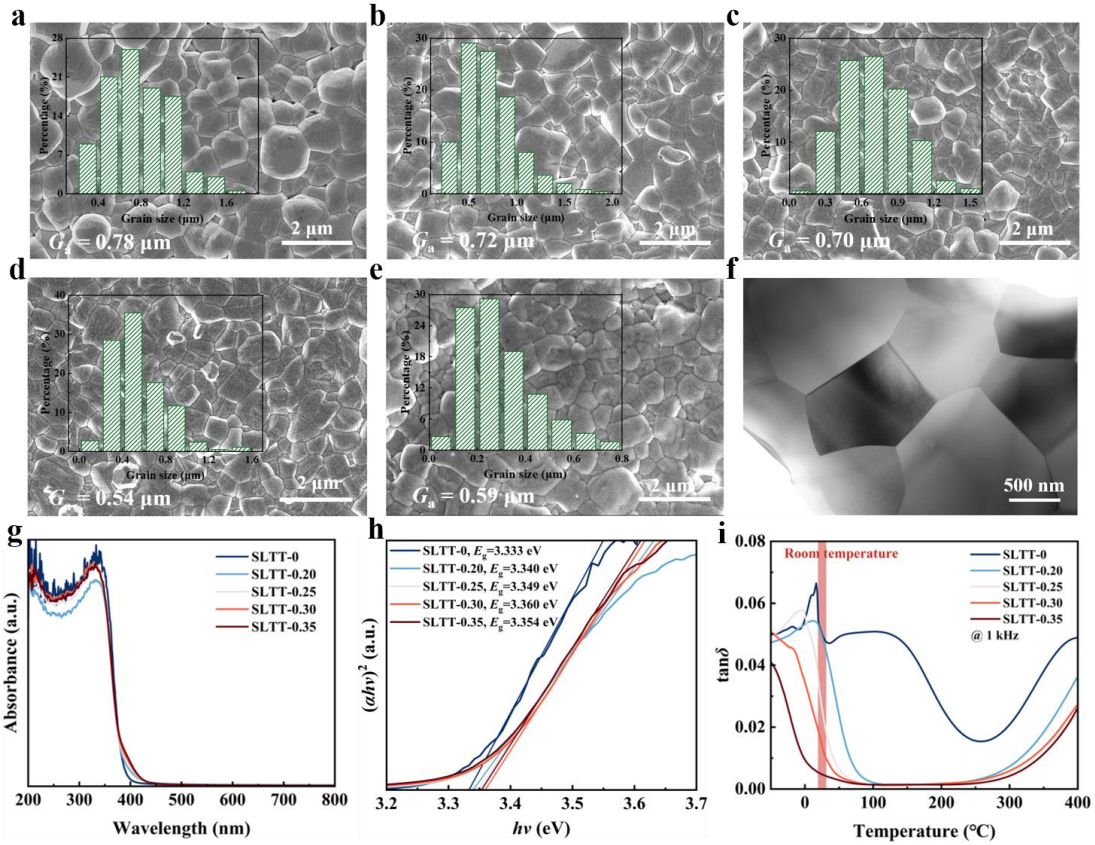

Supplementary Fig. 6 SEM images and corresponding grain size distributions for **a** SLTT-0, **b** SLTT-0.20, **c** SLTT-0.25, **d** SLTT-0.30, and **e** SLTT-0.35. **f** Grain and grain boundary morphology in TEM images for SLTT-0.30 ceramic. **g** UV-vis absorption spectra of SLTT-*x* ceramics. **h** The $(\alpha hv)^2$ as a function of hv for SLTT-*x* ceramics. **i** Temperature-dependent tanδ at 1 kHz. Scanning electron microscope (SEM) images of SLTT-*x* ceramics reveal a progressively homogeneous microstructure. The G_a decreases and then increases with increasing *x*, and the smallest G_a of 0.54 μm is realized in SLTT-0.30 ceramics. TEM image of SLTT-0.30 ceramic show clear and dense grain boundaries, which can inhibit carrier migration. UV-vis absorption spectra are further tested, where E_g can be calculated using the Tauc equation[17]:

$$\alpha hv^2 = A\left(hv - E_g\right) \qquad (10)$$

where α, hv, and A are the absorption coefficient, incident photon energy, and proportionality constant, respectively. SLTT-0.30 ceramics possess the highest E_g of 3.60 eV, indicating that it is difficult for electrons to transition from the valence band to the conduction band, thereby increasing the resistivity. Furthermore, the SLTT-0.30

ceramic maintains an extremely low tanδ over a wide temperature range, and these factors contribute significantly to the high E_b[18].

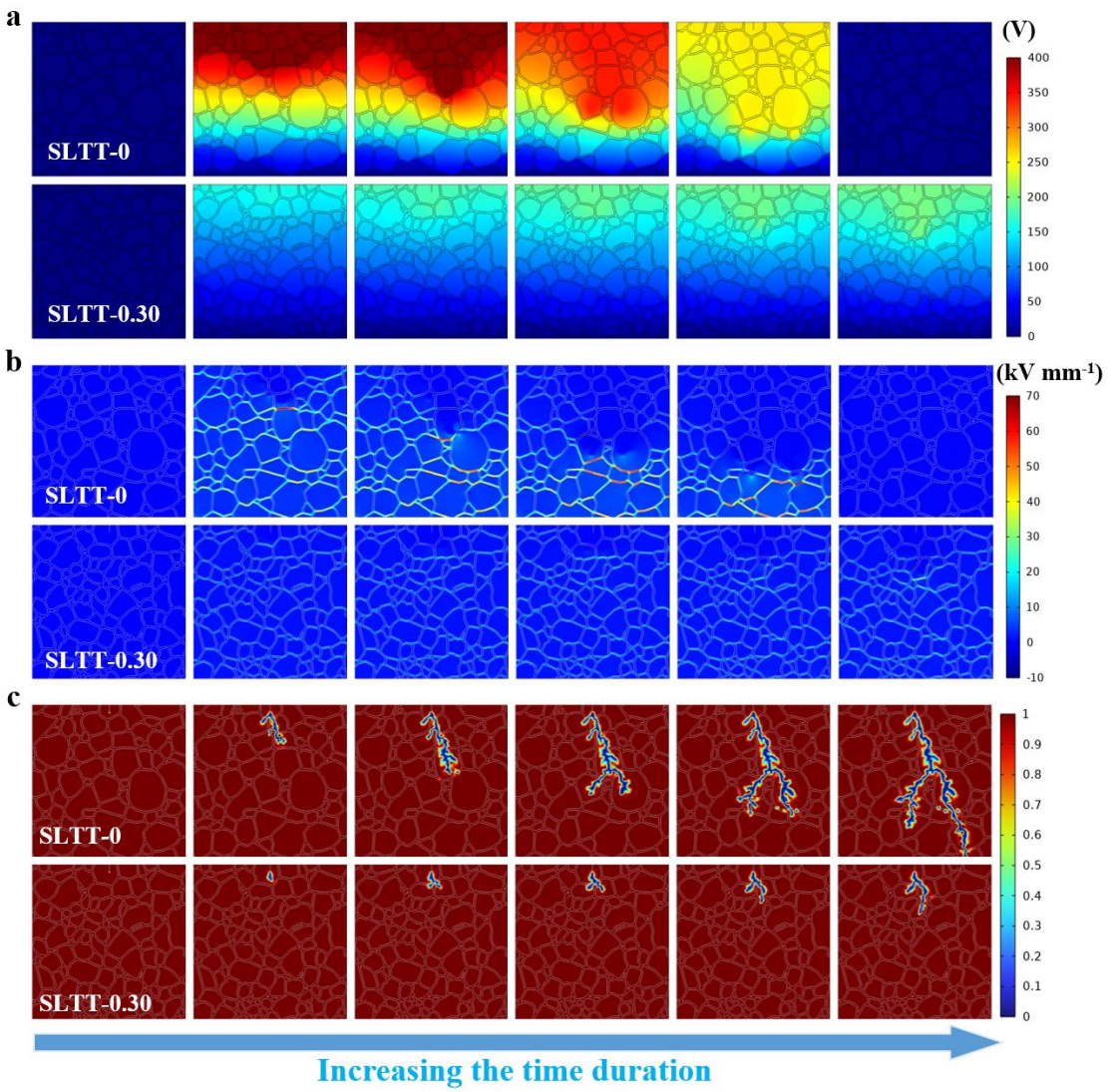

Supplementary Fig. 7 a Simulation of electric potential distributions, **b** Simulation of electric field distributions, and **c** Electrical tree evolution for SLTT-0 and SLTT-0.30 ceramics. The SLTT-0 sample exhibits a large local electric field (red area) and a significant electric potential difference under the applied electric field. Meanwhile, the electric tree grows over time, eventually penetrating the entire model. In contrast, the local electric field and potential difference distribution of the SLTT-0.30 sample tends to be uniform, and the transition between grains and grain boundaries is smoother. In addition, the SLTT-0.30 sample shows significantly impeded electric tree propagation, which can be attributed to the more uniform distribution of grains, higher grain boundary density, and reduced dielectric constant. Together, these factors dissipate energy during the electric tree propagation process, resulting in insensitivity to the electric field[19,20].

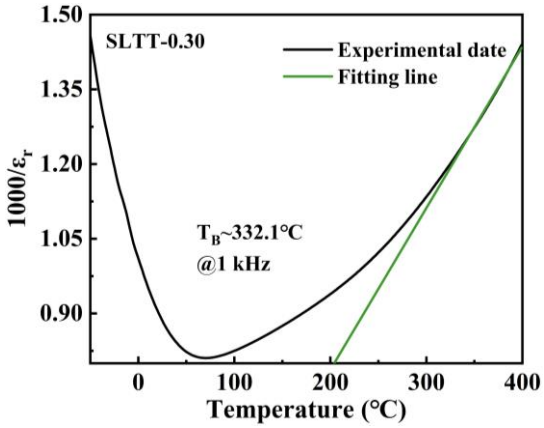

Supplementary Fig. 8 Temperature dependence of the reciprocal of ε_r at 1 kHz to determine T_B for SLTT-0.30 ceramic.

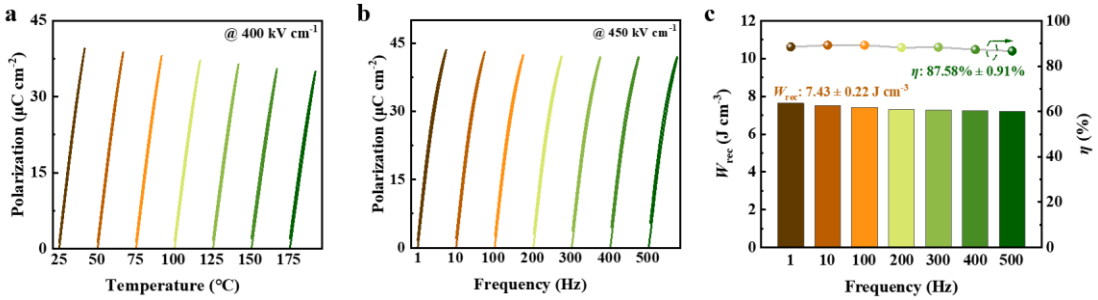

Supplementary Fig. 9 a Temperature-dependent *P-E* loops of SLTT-0.30 at 400 kV cm^{-1}. **b** Frequency-dependent *P-E* loops of SLTT-0.30 at 450 kV cm^{-1}. **c** Frequency-dependent W_{rec} and η of SLTT-0.30 under 450 kV cm^{-1}.

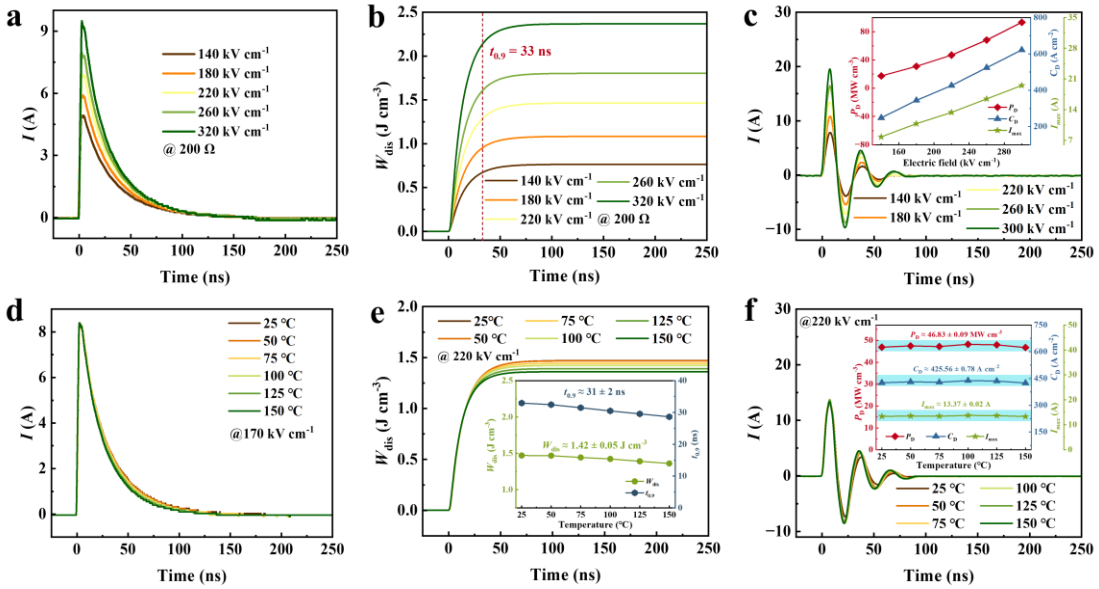

Supplementary Fig. 10 The charge/discharge performance of the SLTT-0.30 ceramic. a Overdamped discharge current curves at different electric fields. **b** W_{dis} as a function of time under different electric fields. **c** Underdamped discharge current curves at different electric fields. The inset shows I_{max}, C_D, and P_D as a function of electric field. **d** Temperature-dependent overdamped discharge current curves. **e** W_{dis} as a function of time under different temperatures. The inset shows W_{dis} and $t_{0.9}$ as a function of temperature. **f** Temperature-dependent underdamped discharge current curves. The inset shows I_{max}, C_D, and P_D as a function of temperature. The discharge energy density W_{dis}, current density C_D and power density P_D can be calculated using the following equations[21]:

$$W_{dis} = R\frac{\int I^2(t)dt}{V} \qquad (11)$$

$$C_D = \frac{I_{max}}{S} \qquad (12)$$

$$P_D = \frac{E \times I_{max}}{2S} \qquad (13)$$

where R, V, and S are the load resistor (200 Ω), volume, and electrode area, respectively.

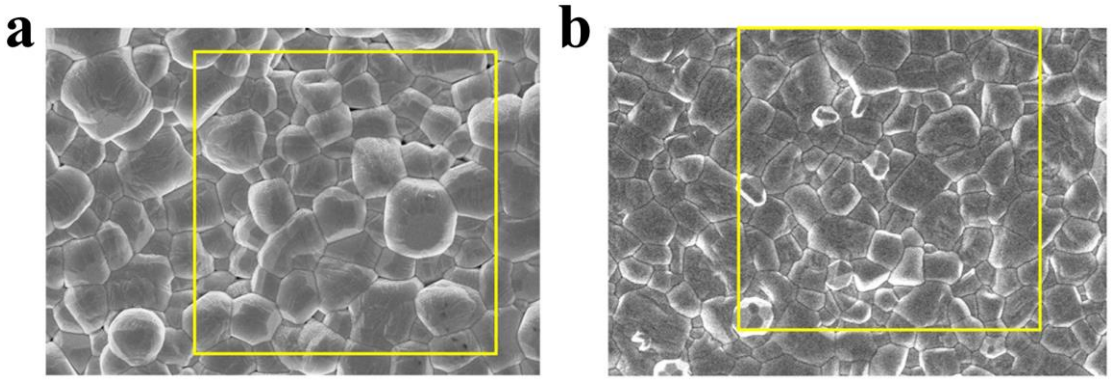

Supplementary Fig. 11 SEM images for finite element simulation, and the yellow boxed areas indicate selected regions. **a** SLTT-0, **b** SLTT-0.30.

Reference

1. Cai, Z. et al. Dielectric response and breakdown behavior of polymer-ceramic nanocomposites: The effect of nanoparticle distribution. *Compos. Sci. Technol.* **145**, 105–113 (2017).
2. Chen, L. et al. Large energy capacitive high-entropy lead-free ferroelectrics. *Nano-Micro Lett.* **15**, 65 (2023).
3. Johnson, K. Variation of dielectric constant with voltage in ferroelectrics and its application to parametric devices. *J. Appl. Phys.* **33**, 2826–2831 (1962).
4. Dong, X. et al. (1-*x*)[0.90NN-0.10Bi($Mg_{2/3}Nb_{1/3}$)O_3]-*x*($Bi_{0.5}Na_{0.5}$)$_{0.7}Sr_{0.3}TiO_3$ ceramics with core–shell structures: a pathway for simultaneously achieving high polarization and breakdown strength. *Nano Energy* **101**, 107577 (2022).
5. Padurariu, L. et al. Field-dependent permittivity in nanostructured $BaTiO_3$ ceramics: modeling and experimental verification. *Phys. Rev. B* **85**, 224111 (2012).
6. Yang, B. et al. Engineering relaxors by entropy for high energy storage performance. *Nat. Energy* **8**, 956–964 (2023).
7. Yang, B. et al. High-entropy enhanced capacitive energy storage. *Nat. Mater.* 21, 1074–1080 (2022).
8. Lu, Z. et al. Superior energy density through tailored dopant strategies in multilayer ceramic capacitors. *Energy Environ. Sci.* **13**, 2938–2948 (2020).
9. Zhu, X. et al. Ultrahigh energy storage density in ($Bi_{0.5}Na_{0.5}$)$_{0.65}Sr_{0.35}TiO_3$-based lead-free relaxor ceramics with excellent temperature stability. *Nano Energy* **98**,

107276 (2022).

10. Zhang, M. et al. Significant increase in comprehensive energy storage performance of potassium sodium niobate-based ceramics via synergistic optimization strategy. *Energy Storage Mater.* **45**, 861–868 (2022).
11. Xie, A. et al. Supercritical relaxor nanograined ferroelectrics for ultrahigh-energy-storage capacitors. *Adv. Mater.* **34**, 2204356 (2022).
12. Che, Z. et al. Phase structure and defect engineering in $(Bi_{0.5}Na_{0.5})TiO_3$-based relaxor antiferroelectrics toward excellent energy storage performance. *Nano Energy* **100**, 107484 (2022).
13. Yan, F. et al. Superior energy storage properties and excellent stability achieved in environment-friendly ferroelectrics via composition design strategy. *Nano Energy* **75**, 105012 (2020).
14. Yan, F. et al. Optimization of polarization and electric field of bismuth ferrite-based ceramics for capacitor applications. *Chem. Eng. J.* **417**, 127945 (2021).
15. Wang, Z. et al. $(Bi_{0.5}Na_{0.5})TiO_3$-based relaxor ferroelectrics with medium permittivity featuring enhanced energy-storage density and excellent thermal stability. *Chem. Eng. J.* **427**, 131989 (2022).
16. Liu, L. et al. Multi-scale collaborative optimization of $SrTiO_3$-based energy storage ceramics with high performance and excellent stability. *Nano Energy* **109**, 108275 (2023).
17. Cao, W. et al. Phase and band structure engineering via linear additive in NBT-ST for excellent energy storage performance with superior thermal stability. *ACS Appl. Mater. Interfaces* **14**, 54051–54062 (2022).
18. Liu, J. et al. Giant comprehensive capacitive energy storage in lead-free quasi-linear relaxor ferroelectrics via local heterogeneous polarization configuration. *J. Mater. Chem. A* **11**, 15931–15942 (2023).
19. Li, X. et al. Simultaneous enhancement of energy storage and hardness performances in $(Na_{0.5}Bi_{0.5})_{0.7}Sr_{0.3}TiO_3$-Based relaxor ferroelectrics via multiscale regulation. *ACS Appl. Mater. Interfaces* **14**, 42245–42257 (2022).
20. Wang, W. et al. Enhancing energy storage performance in $Na_{0.5}Bi_{0.5}TiO_3$-based lead-free relaxor ferroelectric ceramics along a stepwise optimization route. *J. Mater. Chem. A* **11**, 2641–2651 (2023).
21. Chai, Q. et al. Superior energy storage properties and optical transparency in $K_{0.5}Na_{0.5}NbO_3$-Based dielectric ceramics via multiple synergistic strategies. *Small*

19, 2207464 (2023).